

Entrainment of low Mach number thermals in stratified domains

EVAN H. ANDERS,^{1,2} DANIEL LECOANET,^{3,4} AND BENJAMIN P. BROWN^{1,2}

¹*Dept. Astrophysical & Planetary Sciences, University of Colorado – Boulder, Boulder, CO 80309, USA*

²*Laboratory for Atmospheric and Space Physics, Boulder, CO 80303, USA*

³*Princeton Center for Theoretical Science, Princeton, NJ 08544, USA*

⁴*Department of Astrophysical Sciences, Princeton, NJ 08544, USA*

(Received June 3, 2019; Revised ??; Accepted ??)

Submitted to ApJ

ABSTRACT

Large-scale convective flows called giant cells were once thought to transport the Sun’s luminosity in the solar convection zone, but recent observations have called their existence into question. In place of large-scale flows, some authors have suggested the solar luminosity may instead be transported by small droplets of rapidly falling, low entropy fluid. This “entropy rain” would propagate as dense vortex rings, analogous to rising buoyant thermals in the Earth’s atmosphere. In this work, we develop an analytical theory describing the evolution of dense, negatively buoyant thermals. We verify the theory with 2D and 3D simulations of laminar, axisymmetric thermals in highly stratified atmospheres. Our results suggest that entropy rain driven at the surface of the Sun could fall into two categories: a *stalling* regime in which the droplets slow down and expand, and a *falling* regime in which the droplets accelerate and shrink as they propagate downwards. We estimate that solar downflows should be in the falling regime, but should remain large enough to shield their entropic signature until they reach the base of the solar convective zone.

Keywords: hydrodynamics — turbulence — entrainment

1. INTRODUCTION

Recent observations of solar convection have revealed a convective conundrum. Power spectra of horizontal velocities show weaker flows than anticipated at large length scales (Hanasoge et al. 2012; Greer et al. 2015). These observations cast doubt on the existence of giant cells driven by deep convection which should manifest as powerful, large-scale motions at the solar surface. This discrepancy between theory and observations has called into question our fundamental understanding of convection, sparking numerous targeted investigations into the nature of solar convection (Featherstone & Hindman 2016; O’Mara et al. 2016; Cossette & Rast 2016; Käpylä et al. 2017; Hotta 2017).

Rather than appealing to giant cells, Spruit (1997) hypothesized that convective motions in the Sun may be primarily driven by cooling in narrow downflow lanes at

the solar surface. Brandenburg (2016) incorporated this “entropy rain” concept into a non-local mixing length theory, and suggested the entropy rain could take the form of propagating vortex rings. However, Brandenburg (2016) does not include a fundamental aspect of entropy rain: it has lower entropy than the background atmosphere. Entropy rain is dense, and buoyancy forces will modify its dynamics.

It is important to understand how the filling factor of these basic convective elements is affected by their negative buoyancy. In the context of Earth’s atmosphere, “thermals,” or buoyant fluid regions which evolve into rising vortex rings, are thought to be basic unit of convection (e.g., Romps & Charn 2015). Atmospheric thermals are buoyant and rise, but the term is also used for dense, falling fluid. We thus study the entropy rain hypothesis by investigating the evolution of individual dense thermals.

Thermals in the Boussinesq limit have been well studied in the laboratory for decades (see e.g. Morton et al. 1956; Scorer 1957), and more recently through Direct

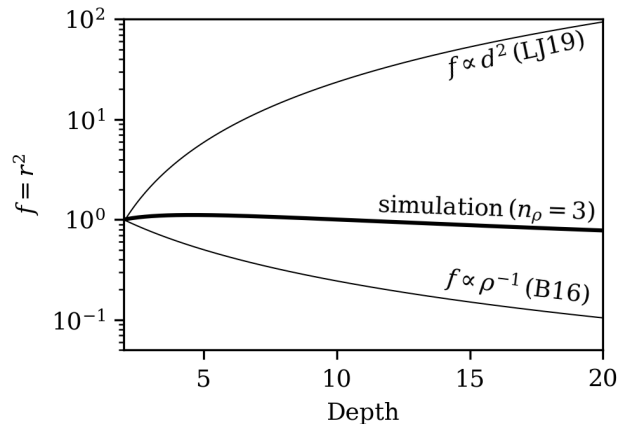


Figure 1. The filling factor of a dense thermal as a function of depth in an atmosphere which spans three density scale heights (the $n_\rho = 3$ case examined later in this work). Thin solid lines are the predictions for filling factor growth for the Boussinesq case (LJ19) and for pure horizontal compression (Brandenburg 2016).

Numerical Simulation (DNS) (Lecoanet & Jeevanjee 2018). These studies find that thermals expand radially and decelerate as they propagate. Such an expansion may prevent entropy rain from reaching the bottom of the solar convection. However, this work does not include the effects of density stratification.

Ignoring entropy variations, Brandenburg (2016) suggests the filling fraction f of entropy rain should decrease like $f \propto \rho^{-1}$ for horizontal compression and $f \propto \rho^{-2/3}$ for spherical compression. On the other hand, the filling factor of Boussinesq thermals *increases* like $f \propto d^2$, where d is the depth of the thermal. These regimes are shown in Fig. 1, and compared to the true propagation of a numerically simulated dense thermal including both entropy variations and density stratification.

In this paper, we extend Lecoanet & Jeevanjee (2018) (hereafter LJ19) to study the propagation of low-Mach number, low-entropy thermals in stratified domains. We are specifically interested in how the buoyancy force affects the scaling of the thermal radius, or filling factor, with depth. If buoyancy dominant, it is possible that entropy rain would simply grow too large and stall before reaching the bottom of the solar convection zone. On the other hand, if the compression effects of Brandenburg (2016) are dominant, then these thermals could propagate to the bottom of the solar convection zone, validating the entropy rain picture.

In section 2, we develop a theoretical description of thermals in a stratified domain. In section 3, we describe the numerical experiments conducted in this work. In section 4, we compare our theory and simulation results.

Finally, in section 5, we discuss what our results imply for the entropy rain hypothesis.

2. MODEL OF THERMAL EVOLUTION

2.1. Phenomenological description of thermal evolution

Fig. 2 depicts the descent of 3D cold thermals released from rest in domains which span a different number of density scale heights (n_ρ). The left panel shows a weakly stratified domain with $n_\rho = 0.5$, whereas the right panel shows a strongly stratified domain with $n_\rho = 3$. In both cases, the thermal is initialized with a spherical negative entropy perturbation, which a diameter of 5% of the domain depth. This dense sphere spins up into an axisymmetric vortex ring, and the vertical cross section through this vortex ring shows two circular vorticity and entropy extrema. In the $n_\rho = 0.5$ simulation, the thermal grows with depth, similar to thermals in the Boussinesq regime. On the other hand, in the $n_\rho = 3$ simulation, the thermal’s radius remains approximately constant.

The goal of this paper is to understand the evolution of the thermal in the vortex ring stage. All of the thermals studied in this work are laminar, similar to the Hill vortices studied by Brandenburg (2016). Crucially, LJ19 showed little difference between the evolution of laminar and turbulent thermals in the Boussinesq limit. As a result, we leave studies of turbulent thermals in stratified domains for future work.

In the following sections, we will use the impulse of dense vortex rings derive their depth and radii with time.

2.2. Impulse

The evolution of thermals in the Boussinesq limit has been understood for decades (see e.g., LJ19 for a description and references). While many theoretical descriptions rely on self-similarity arguments, we will show how the impulse of a thermal controls its evolution.

The hydrodynamic impulse is defined as (Shivamoggi 2010),

$$\mathbf{I} = \frac{1}{2} \int_{\mathcal{V}} \mathbf{x} \times (\nabla \times (\rho \mathbf{u})) dV, \quad (1)$$

where \mathbf{x} is the position vector. The impulse is the time-integrated work which has acted on the fluid to result in the current fluid motion. It is thus unaffected by internal forces (e.g., pressure or viscous). Upon integration by parts, it is obvious that the impulse encompasses the momentum of the fluid within the volume \mathcal{V} . However, one can also show that the surface terms correspond to the momentum outside the volume \mathcal{V} (e.g. Akhmetov 2009). A thermal with volume \mathcal{V} , density ρ , and translating with velocity $w_{\text{th}} \hat{z}$ thus has an impulse

$$I_z = (1 + k) \rho \mathcal{V} w_{\text{th}}, \quad (2)$$

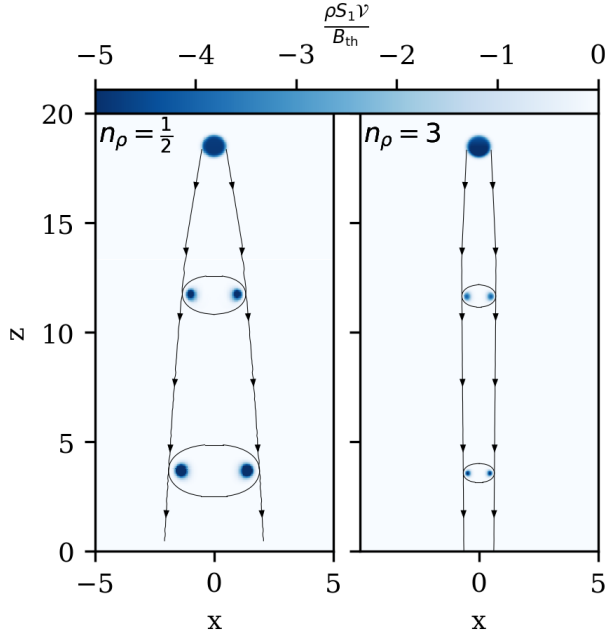


Figure 2. The mass-weighted entropy perturbation, $\rho S_1 r^3$, for two thermals. (left) a thermal in a weakly stratified domain with $n_\rho = 1/2$ density scale heights; (right) a thermal in a strongly stratified domain with $n_\rho = 3$. While both start with precisely the same initial condition, the thermal in low stratification expands with depth, whereas the thermal in strong stratification compresses with depth.

where k is due to the “virtual mass effect” from the environmental fluid moving together with the thermal (Tarshish et al. 2018).

We now restrict our study to an ideal gas in the low Mach-number regime, in an adiabatic background. Due to rapid pressure equilibration in for low Mach-number flows, we can approximate [Don't know if this is actually a good idea...](#)

$$\frac{\rho_1}{\rho_0} \approx \frac{S_1}{c_P},$$

where S_1 is the specific entropy perturbation and c_P is the specific heat at constant pressure; thermodynamic variables are decomposed into background (subscript 0) and fluctuating (subscript 1) components.

The rate of change of change of the impulse is

$$\frac{d\mathbf{I}}{dt} = \int_V \rho_1 \mathbf{g} dV,$$

because the surface terms completely cancel. It is useful to define the buoyancy perturbation,

$$B \equiv \int_V \rho S_1 \frac{g}{c_P} dV. \quad (3)$$

such that

$$\frac{dI_z}{dt} = B. \quad (4)$$

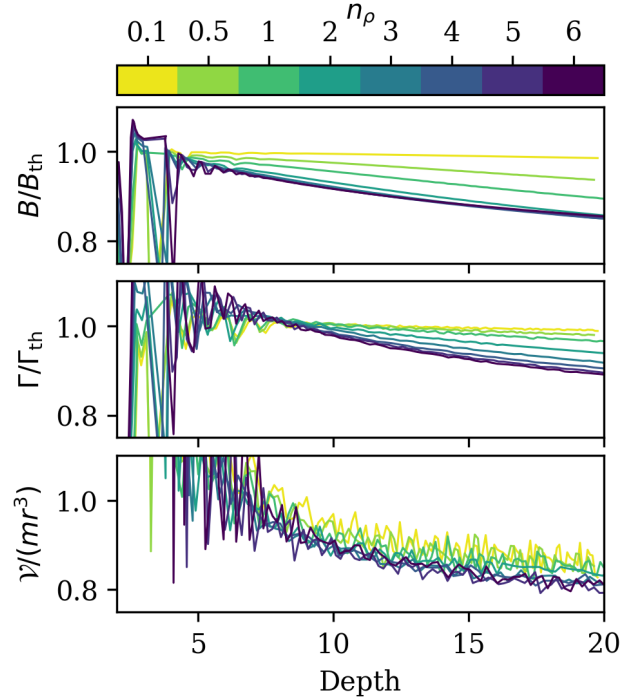


Figure 3. Evolution of circulation, buoyancy perturbation, and volume factor in thermal simulations. All are nearly constant after an initial spin-up phase. With increasing stratification, we see marginally more detrainment (middle panel). The volume factor can be approximated to be $\mathcal{O}(7)$ for all of our simulations.

In the limit of a low Mach-number, thin-core vortex ring, the impulse can be approximated as

$$I_z \approx \pi \rho r^2 \Gamma, \quad (5)$$

where r is the radius of the thermal from its axis of symmetry to its vorticity maximum, and $\Gamma = \int_{\mathcal{A}} (\nabla \times \mathbf{u}) dA$ is the circulation in a cross-section of the vortex ring. The circulation can change due to baroclinic torques,

$$\frac{d\Gamma}{dt} = \oint_{\mathcal{C}} g \frac{S_1}{c_P} \hat{z} \cdot d\mathbf{x}, \quad (6)$$

where $\mathcal{C} = \partial\mathcal{A}$ is the contour around the thermal’s vorticity. For the case of a vortex core in which the entropy perturbation is contained tightly in the core, as in Fig. 2, a contour can be drawn for which $S_1 \approx 0$. Thus, there are no net baroclinic torques, and we will treat the circulation of a developed vortex ring as a conserved quantity.

2.3. Model of thermal evolution

After spinning up, we assume that the thermal has a negative buoyancy, B_{th} , and circulation, Γ_{th} . While these thermals began as initial spherical perturbations,

they act like vortex rings which evolved from a “virtual origin” where the vortex ring had zero radius. From this virtual origin, the vortex ring’s impulse would have been I_0 at time $t = 0$ when the true thermal is released from rest.

We find the thermal undergoes weak detrainment, so the negative buoyancy of the thermal decreases slightly in time (Fig. 3b). We thus express the buoyancy perturbation as

$$B \approx \chi B_{\text{th}}, \quad (7)$$

where χ is a constant of $\mathcal{O}(1)$ which represents this detrainment. We then integrate Eqn. 4,

$$I_z = \chi B_{\text{th}} t + I_0.$$

Combining this with Eqn. 5, we retrieve our first main result,

$$r = \sqrt{\frac{\chi B_{\text{th}} t + I_0}{\pi \rho \Gamma_{\text{th}}}}. \quad (8)$$

Recall there are no net baroclinic torques, so stays Γ_{th} nearly constant (Fig. 3a). In the Boussinesq limit where $\rho \rightarrow \text{constant}$, we retrieve the $r \propto \sqrt{t}$ scaling found in LJ19. In the limit of strong stratification, $r \propto \rho^{-1/2}$, corresponding to purely horizontal compression, with $r^2 \propto \rho^{-1}$ (Brandenburg 2016).

To solve for the vertical evolution of the thermal, we can use equation 2. We approximate the volume as $\mathcal{V} = m r^3$, where m is a parameter which we take to be constant. We find

$$\rho^{-1/2} w_{\text{th}} = \left(\frac{(\pi \Gamma_{\text{th}})^{3/2}}{(1+k)m} \right) (\chi B_{\text{th}} t + I_0)^{-1/2}. \quad (9)$$

Defining the thermal velocity $w_{\text{th}} \equiv dz_{\text{th}}/dt$, and assuming I_0 is small, we have

$$\frac{dz_{\text{th}}}{\rho(z_{\text{th}})^{1/2}} = \left(\frac{(\pi \Gamma_{\text{th}})^{3/2}}{m(1+k)(\chi B_{\text{th}})^{1/2}} \right) \frac{dt}{t^{1/2}}. \quad (10)$$

This can be easily integrated given an atmospheric stratification $\rho(z)$.

To summarize, we model thermals as thin-core vortex rings. The vortex ring is parameterized by its buoyancy perturbation and circulation, which are assumed to be nearly constant after spin-up. The impulse increases in magnitude due to buoyancy forces (Eqn. 4), and allows us to relate the size of the vortex ring (Eqn. 5) to the momentum of the thermal and its ambient fluid (Eqn. 2). Assuming the thermals’ volume is spheroidal and that the virtual mass effect and detrainment can be parameterized as constants, we arrive at Eqn. 10.

2.4. Solution polytrope atmospheres

In this work, we study an ideal gas with an adiabatic index of $\gamma = 5/3$. An adiabatic polytrope satisfies

$$T_0 = 1 + (\nabla_{\text{ad}})(z - L_z), \quad (11)$$

$$\rho_0 = T_0^{n_{\text{ad}}}, \quad (12)$$

where $n_{\text{ad}} = (\gamma - 1)^{-1}$. All thermodynamic quantities are nondimensionalized such that $\rho_0 = T_0 = 1$ at $z = L_z$, the top of the domain.

Integrating Eqn. 10 under this polytropic density stratification, we find

$$z_{\text{th}} = \nabla_{\text{ad}}^{-1} \left[\left(\frac{2C}{\alpha} \sqrt{t + t_{\text{off}}} + T_{\text{th},0}^{1/\alpha} \right)^\alpha - 1 \right] + L_z, \quad (13)$$

where $C \equiv \pi^{3/2} \nabla_{\text{ad}} / (1+k) / m \sqrt{\Gamma_{\text{th}}^3 / (\chi B_{\text{th}})}$ and the temperature at the virtual origin is $T_{\text{th},0} = 1 + \nabla_{\text{ad}}(z_{\text{th},0} - L_z)$. The thermal is at the virtual origin, $z = z_0$, at time $t = -t_{\text{off}}$. The constant $\alpha^{-1} = 1 - n_{\text{ad}}/2$, and in the limit of large stratification, we find that $z_{\text{th}} \propto t^2$ for our case of $\alpha = 4$.

In our simulations, the thermal is initialized as a uniform sphere of dense fluid but it quickly spins up into a vortex ring. While we do not attempt to model the spin-up phase in this paper, it can be parameterized by the buoyancy B_{th} , circulation Γ_{th} , as well as the virtual origin $z_{\text{th},0}$, and temporal offset t_{off} . Our theory also involves the volumetric aspect ratio of the thermal f , the detrainment fraction χ , and the effective buoyancy k . These appear to be only weakly dependent on the stratification for the thermals we have simulated.

3. SIMULATION SETUP

To test our theory, we run a series of simulations of the 3D fully compressible equations, as well as 2D simulations of the anelastic equations. We verify the 3D and 2D simulations produce the same results when run with the same parameters. Because 2D simulations are less computationally expensive, we cover a broader parameter regime.

While solar convection is very turbulent, we restrict our study to laminar thermals. In the Boussinesq limit, LJ19 showed the evolution of turbulent vortex rings is well described by laminar theory; we expect this will also hold in the stratified case. In future work, we will apply this laminar theory to turbulent thermals with density stratification, which necessitates 3D simulations.

3.1. 2D Anelastic Simulations

The LBR anelastic equations are (Lecoanet et al. 2014),

$$\nabla \cdot \mathbf{u} = -w \partial_z \ln \rho_0, \quad (14)$$

$$\begin{aligned} \partial_t \mathbf{u} + \mathbf{u} \cdot \nabla \mathbf{u} = \\ -\nabla \varpi + S_1 \hat{z} + \frac{1}{\rho_0 \text{Re}} \left[\nabla^2 \mathbf{u} + \frac{1}{3} \nabla (\nabla \cdot \mathbf{u}) \right] \end{aligned} \quad (15)$$

$$\begin{aligned} \partial_t S_1 + \mathbf{u} \cdot \nabla S_1 = \\ \frac{1}{\text{Re}} \left(\frac{1}{\text{Pr} \rho_0 c_P} [\nabla^2 S_1 + \partial_z \ln T_0 \cdot \partial_z S_1] \right. \\ \left. + \frac{-(\nabla_{\text{ad}})}{\rho_0 T_0} \sigma_{ij} \partial_{x_i} u_j \right), \end{aligned} \quad (16)$$

where $\bar{\sigma}$ is the viscous stress tensor in units of inverse time. We solve these equations in cylindrical geometry, assuming axisymmetry.

Following LJ19, we non-dimensionalize the equations with the initial diameter of the thermal and its freefall velocity. These equations are then fully specified in terms of the Reynolds number and Prandtl number,

$$\text{Re} = \frac{u_{\text{th}} L_{\text{th}}}{\nu}, \quad \text{Pr} = \frac{u_{\text{th}} L_{\text{th}}}{\chi}, \quad u_{\text{th}}^2 = \frac{g L_{\text{th}} \Delta s}{c_P}, \quad (17)$$

where u_{th} is the freefall velocity, L_{th} is the thermal length scale, and Δs is the magnitude of the specific entropy signature of the thermal.

The background density and temperature are given by Eqs. 11 & 12. The adiabatic temperature gradient is $\nabla_{\text{ad}} = g(e^{n_\rho/n_{\text{ad}}} - 1)/(L_z c_P)$, where $L_z = 20$ is the height of the domain.

We choose an atmospheric model in which the dynamic viscosity, $\mu = \rho_0 \nu$, and the thermal conductivity, $\kappa = \rho_0 \chi$, are both uniform and constant in time. We make this choice as the mass-weighted diffusivities, μ and κ , appear in the density-weighted momentum and entropy equations, and we find the density-weighted entropy and momentum to be key quantities in our thermal theory. The diffusivities ν and χ therefore scale inversely with the density. As the diffusivities scale with depth, Re is specified at the thermal's initial depth. All simulations conducted in this work use a value of $\text{Re} = 600$ and $\text{Pr} = 1$.

3.2. 3D Fully Compressible Simulations

In order to verify our 2D anelastic simulations, we also simulate thermals with the 3D Navier Stokes equations. We use the $(T, \ln \rho)$ formulation of the equations

(Lecoanet et al. 2014; Anders & Brown 2017),

$$\frac{\partial \ln \rho_1}{\partial t} + \epsilon^{-1} (\mathbf{u} \cdot \nabla \ln \rho_0 + \nabla \cdot \mathbf{u}) = -\mathbf{u} \cdot \nabla \ln \rho_1, \quad (18)$$

$$\begin{aligned} \frac{\partial \mathbf{u}}{\partial t} + \nabla T_1 + T_1 \nabla \ln \rho_0 + T_0 \nabla \ln \rho_1 = \\ -\epsilon T_1 \nabla \ln \rho_1 + \frac{1}{\rho \text{Re}} \left[\nabla^2 \mathbf{u} + \frac{1}{3} \nabla (\nabla \cdot \mathbf{u}) \right] \\ \frac{\partial T_1}{\partial t} + \epsilon^{-1} [\mathbf{u} \cdot \nabla T_0 + (\gamma - 1) T_0 \nabla \cdot \mathbf{u}] = \\ -[\mathbf{u} \cdot \nabla T_1 + (\gamma - 1) T_1 \nabla \cdot \mathbf{u}] + \frac{1}{\rho c_V \text{Re}} \left[\frac{1}{\text{Pr}} \nabla^2 T_1 + \sigma_{ij} \partial_{x_i} u_j \right]. \end{aligned} \quad (19)$$

These equations are non-dimensionalized in the same way as the anelastic equations, and use the same background atmosphere. The new parameter $\epsilon = u_{\text{th}}^2$ is the magnitude of entropy perturbations and sets the Mach number of the thermal flows; we use $\epsilon = 10^{-4}$ in this work.

3.3. Initial conditions

The simulations is initialized with a spherical specific entropy perturbation,

$$S_1 = \frac{1}{2} \left[\text{erf} \left(\frac{r' - r_{\text{th}}}{\delta} \right) - 1 \right]. \quad (21)$$

Here, $r' = \sqrt{r^2 + (z - z_0)^2}$, where $z_0 = L_z - 3r_{\text{th}}$, with the thermal radius set as $r_{\text{th}} = 0.5$, and a smoothing width, $\delta = 0.1$. As mentioned previously, $\text{Re} = 600$ and $\text{Pr} = 1$ are specified at the thermal's initial depth, $z = z_0$.

For the fully compressible simulations, we must also specify the density perturbation ρ_1 . We pick perturbations that are in pressure equilibrium,

$$\ln \rho_1 = S_1 / c_P, \quad T_1 = T_0 (e^{-\epsilon \ln \rho_1} - 1) / \epsilon. \quad (22)$$

3.4. Numerics

We simulate the thermals using the Dedalus¹ pseudospectral framework (Burns et al. 2016, 2019). The 2D simulations use using an implicit-explicit (IMEX), third-order, four-stage Runge-Kutta timestepping scheme RK443 (Ascher et al. 1997), and the 3D simulations use the second-order semi-implicit backward differentiation formulation SBDF2 (Wang & Ruuth 2008).

The 2D simulation domain is the direct product of a Fourier basis ($z \in [-L_z/4, L_z]$) and a Chebyshev basis ($r \in [0, L_r]$). The boundary conditions are $\partial_r S_1 = w =$

¹ <http://dedalus-project.org/>

$(\nabla \times \mathbf{u})_\phi = 0$ at $r = L_r$, and the regularity of the equations automatically impose $u = \partial_r(w) = \partial_r(S_1) = 0$ at $r = 0$. The 3D simulation domain is the direct product of Fourier bases in the horizontal directions ($x, y \in [-L_r, L_r]$) and a Chebyshev basis ($z \in [0, L_z]$). We impose impenetrable, stress free, fixed-temperature boundary conditions at the upper and lower boundaries. In all of our simulations we specify $L_z = 20$ and $L_r = 5$. We extend our 2D simulation domains to $z = -L_z/4$ because those simulations are vertically periodic. This extension allows us to study the full transit of the thermal above $z = 0$ and terminate the simulation before it begins to wrap through the bottom of the periodic domain.

All of the code used to perform the simulations in this work can be found online in the supplementary materials in a Zenodo repository (CREATE AND CITE REPO).

4. MODEL VERIFICATION

To compare to the model, we must measure the thermal's depth and radius. We define the thermal's depth and radius using the thermal's entropy minimum. For specifics on how these measurements are conducted in our simulations, we refer the reader to appendix A.

In Fig. 4a, we show the depth $d_{\text{th}} = L_z - z_{\text{th}}$ of the thermal as a function of time for simulations with different stratifications. At very low stratification (e.g., $n_\rho = 0.1$), the thermal is small compared to the local density scale height at all depths, and it evolves roughly according to the Boussinesq prediction of $d \propto \sqrt{t}$. As the stratification increases, the thermal transits the domain more quickly and approaches the limit of $d \propto t^2$ predicted in the highly stratified limit of Eqn. 13. The theoretical fits for depth from the prediction of Eqn. 13 are plotted over the measured data. The theoretical fits are poor at early times when the thermal is spinning up from its initial spherical state into the vortex ring state. Once the thermal is spun up into a vortex ring, the theory shows remarkable agreement with the data.

In Fig. 4b, we show the corresponding thermal velocity as a function of depth. Low density ($n_\rho = 0.1$) thermals decelerate with depth. With increasing stratification, this deceleration stops and sufficiently stratified runs ($n_\rho \geq 3$) experience acceleration.

Fig. 5a plots the thermal radius as a function of depth. In the low stratification limit, the radius of the thermal grows linearly with depth, $r \propto d$, as is the case in the Boussinesq limit (LJ19). The growth of the thermal is due to entrainment of environmental fluid, which causes the thermal to decelerate like $w \propto d^{-1}$, as is shown in Fig. 4b. However, as stratification increases, the thermal entrainment of environmental fluid decreases and it

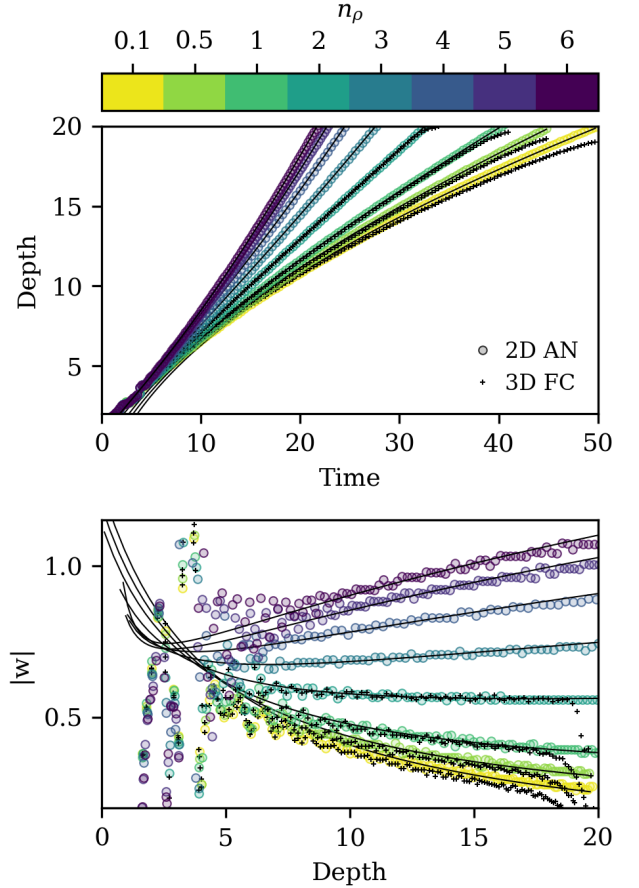


Figure 4. (a) The thermal depth as a function of time for the 2D anelastic and 3D fully compressible simulations. (b) The corresponding thermal velocities as a function of depth. Theoretical predictions from section 2 are plotted in thin solid lines for each case (see parameters in table 1).

experiences less expansion. In the limit of large stratification ($n_\rho \geq 3$), thermals contract with depth, and the thermals accelerate as they fall.

Finally, we quantify the excellent agreement between the 2D anelastic and 3D fully compressible simulations in Fig. 5b. We ran simulations in both models for $n_\rho = [0.5, 1, 2]$. There are slight discrepancies early in the simulation, when the thermal is spinning up, and late in the simulation, when the simulations begin interacting with the bottom of the domain. Outside these times, we find differences in the radius of less than 1%. This gives us confidence that our high stratification anelastic simulations are producing reliable results. Lecoanet et al. (2014) also found close agreement between low Mach-number anelastic and fully compressible simulations.

The values of the parameters described in section 2 for each of our simulations are presented in table 1. As

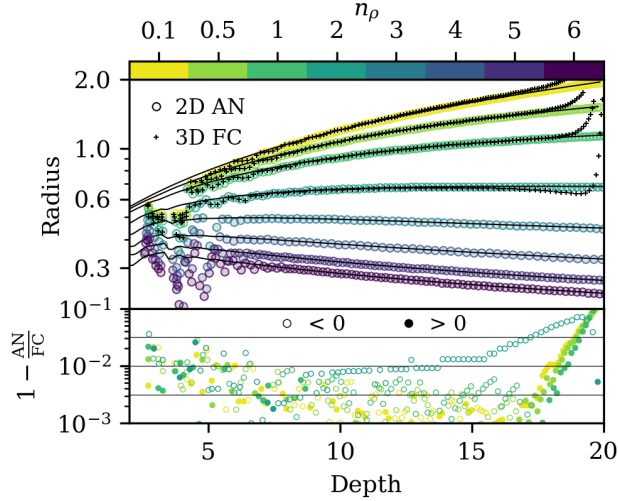


Figure 5. (a) Thermal radius as a function of depth are plotted for the 2D anelastic and 3D fully compressible simulations. Theoretical predictions from section 2 are plotted in thin solid lines. (b) The fractional difference between anelastic and fully compressible simulations.

anticipated, k is $\mathcal{O}(0.5)$ and χ is $\mathcal{O}(1)$, with both decreasing slightly in value with increasing stratification, consistent with Fig. 3. In all cases, the buoyancy B_{th} is similar to the integrated buoyancy in the initial conditions, with some losses due to detrainment in the spin-up. We also find that the non-dimensional circulation is $\mathcal{O}(-2)$ for each of our cases, and decreases with increasing stratification.

5. DISCUSSION & CONCLUSION

In this paper we developed a simple theory of the evolution of negatively buoyant vortex rings in stratified atmospheres. We showed that this theory predicts that dense thermals will experience less entrainment than boussinesq thermals due to increasing atmospheric density with depth. We performed 2D anelastic simulations of thermal evolution for varying degrees of stratification and showed that our parameterized theory describes the evolution of thermals in these systems remarkably well. Furthermore, we verified the validity of our anelastic simulations with select 3D fully compressible simulations of thermal evolution and found agreement to under 1%.

We note that the evolution of dense thermals in stratified domains is complex, and neither the assumption of horizontal compression (as in e.g., Brandenburg 2016) or the evolution of thermals in the Boussinesq regime (as in LJ19) fully describes the behavior of these events fully. Rather, results fall somewhere in between, and theory

and simulations suggest that there are two regimes of downflowing thermal behavior:

1. A low-stratification “stalling” regime, in which the thermal entrains environmental fluid and slows down, acting much like the Boussinesq regime, and
2. A high-stratification “falling” regime, in which the thermal falls fast enough that compression due to the atmospheric stratification results in minimal entrainment and the thermal accelerates as it falls deeper into the atmosphere.

However, we note that both the falling and stalling regimes observed here could result in interesting problems for the entropy rain hypothesis. If solar convection were comprised of thermals in the stalling regime, such convective elements would grow enormously in size and slow down very close to the solar surface. In a perfectly quiescent atmosphere, these very slow, very large convective elements would propagate to the base of the convection zone over enormous timescales, but their large length scales would likely shield them from any dissipative effects. However, the solar convection zone is highly turbulent, and we expect that any large, coherent, and slowly propagating structures would be torn apart by turbulent motions.

On the other hand, if solar convection is comprised of thermals in the falling regime, then it is not out of the question for solar surface elements to reach deep into the Sun. Such vortex rings in the falling regime would theoretically be able to reach the bottom of the solar convection zone, and the effects of buoyancy which counteract some of the natural compressional effects of the atmosphere, could shield the thermal from dissipative effects. In the absence of this buoyant expansion, we anticipate that falling vortices in the solar convection zone would shrink to the point where conductivity could become important. However, due to the presence of buoyant entrainment, thermals in nature are likely shielded from conductive effects.

In order to determine what behavioral regime thermals would occupy in the Sun, we will now estimate which of the simulations presented in this work could most accurately describe entropy rain in the Sun. We estimate that thermal diameters would be roughly the width of solar downflows, or $L = 0.1$ Mm. Using the VAL atmosphere of Avrett & Loeser (2008), we estimate the solar surface to have a temperature of $T_0 = 6000$ K, a density of $\rho_0 = 1.74 \times 10^{-7}$ g/cm³, a sound speed of $c_s = 9.5 \times 10^5$ cm/s, and the average density over the radial extent of the thermal is $\bar{\rho} = 1.17\rho_0$. Estimating that solar downflows have a temperature deviation of $T_1 = -500$ K (Borrero & Bellot Rubio 2002), the

Table 1. Simulation output parameterization

| n_ρ | $z_{\text{th},0}$ | t_{off} | B_{th} | Γ_{th} | m | χ | k |
|--|-------------------|------------------|-----------------|----------------------|------|--------|-------|
| 2D Anelastic Simulations | | | | | | | |
| 0.1 | 24.6 | 0.144 | -0.548 | -2.17 | 8.05 | 1.04 | 0.732 |
| 0.5 | 24.2 | 0.695 | -0.569 | -2.12 | 8.34 | 0.977 | 0.715 |
| 1 | 23.7 | 1.11 | -0.602 | -2.05 | 8.65 | 0.915 | 0.703 |
| 2 | 22.3 | 1.27 | -0.713 | -1.89 | 9.23 | 0.842 | 0.682 |
| 3 | 21.2 | 1.01 | -0.947 | -1.73 | 9.81 | 0.807 | 0.654 |
| 4 | 20.5 | 0.615 | -1.47 | -1.59 | 10.2 | 0.794 | 0.642 |
| 5 | 20.0 | 0.425 | -2.70 | -1.49 | 10.7 | 0.781 | 0.609 |
| 6 | 19.8 | 0.041 | -5.73 | -1.43 | 10.8 | 0.787 | 0.616 |
| 3D Fully Compressible Simulations | | | | | | | |
| 0.1 | 23.4 | -0.337 | -0.547 | -2.17 | 8.98 | 1.06 | 0.636 |
| 0.5 | 23.8 | 0.572 | -0.568 | -2.12 | 8.79 | 0.978 | 0.678 |
| 1 | 23.6 | 1.15 | -0.601 | -2.05 | 8.87 | 0.907 | 0.689 |
| 2 | 22.9 | 2.88 | -0.699 | -1.89 | 9.24 | 0.776 | 0.706 |

NOTE—

nondimensional entropy signature of solar downflows is $S_1/c_p \sim \gamma^{-1} \ln(1+T_1/T_0) = -5.22 \times 10^{-2}$. Using a solar surface gravity value of $g = 2.74 \times 10^4 \text{ cm/s}^2$, the buoyancy of such a thermal is $\tilde{B} \approx (4\pi/3)(L/2)^3 \bar{\rho} g (S_1/c_p) = -1.52 \times 10^{17} \text{ g cm}^4/\text{s}^2$. Nondimensionalizing this by $N = (S_1/c_p)L^2 u_{\text{th}}^2 \rho_0$ with $u_{\text{th}} = c_s \sqrt{S_1/c_p}$, we find $B = \tilde{B}/N = -3.57$, which lies between the $n_\rho = 5$ and $n_\rho = 6$ simulations we studied here.

We assume that our estimate for B could be off by a factor of two, and thus bracket the behavior of solar thermals as having $[B_\ell, B_u] = 0.5B, 2B$. Interpolating and extrapolating the data in Table 1, we calculate theoretical predictions for how thermals with these buoyancies would evolve in the solar convection zone. We plot these estimates of thermal evolution in the solar convection zone in Fig. 6, using a simple solar interior model calculated using MESA (Paxton et al. 2011) to map the density profiles of our simulation domains onto the density profile of the Sun. In Fig. 6a&b, we respectively show the evolution of these thermals’ radii and velocities inside of the Sun, and compare their evolution to pure horizontal compression. We use the solar diffusivity models shown in Brown (2011) to estimate the timescale over which the thermal would diffuse its entropy signature ($\tau_\kappa = \chi/r^2$) and the thermal freefall timescale over 1 Mm ($\tau_{\text{ff}} = (1 \text{ Mm})/w_{\text{th}}$). In Fig. 6c, we plot the ratio of these two timescales over the thermal’s evolution.

In general, we find that our entire estimated window for our thermals exists in the falling regime and these thermals experience radial compression with corresponding increases in velocity. Furthermore, through-

out the thermal’s fall, we find that $\tau_\kappa \gg \tau_{\text{ff}}$, and thus we do not expect the thermal to diffuse its entropic signature. We find a fractional diffusion rate over the thermal’s transit of the solar convection zone of $\int_{R_\odot}^{0.7R_\odot} \tau_\kappa^{-1} dR/w_{\text{th}} = [6.55, 1.57] \times 10^{-3}$ for $[B_\ell, B_u]$. In other words, throughout our bracketing interval, we estimate that the thermal loses less than 1% of its entropic signature to diffusion. We similarly estimate the amount of entropy that the thermal should lose due to viscous heating as $(S_1/c_p)^{-1} \int_{R_\odot}^{0.7R_\odot} \nu w_{\text{th}}^2 / (r^2 \rho T c_p) dr/w_{\text{th}} = [1.17, 0.17] \times 10^{-4}$ for $[B_\ell, B_u]$.

“Entropy rain” is the hypothesis that narrow downflows can transport the luminosity of the Sun via enthalpy fluxes. If the rain’s entropy diffuses away before it hits the bottom, then it cannot transport the flux. We find that with our more accurate model for thermal propagation, the thermal maintains its entropy all the way to the base of the convection zone, and entropy rain is a possible mechanism for transporting the solar luminosity.

This work was supported by NASA Headquarters under the NASA Earth and Space Science Fellowship Program – Grant 80NSSC18K1199. This work was additionally supported by NASA LWS grant number NNX16AC92G. Computations were conducted with support by the NASA High End Computing (HEC) Program through the NASA Advanced Supercomputing (NAS) Division at Ames Research Center on Pleiades with allocation GID s1647.

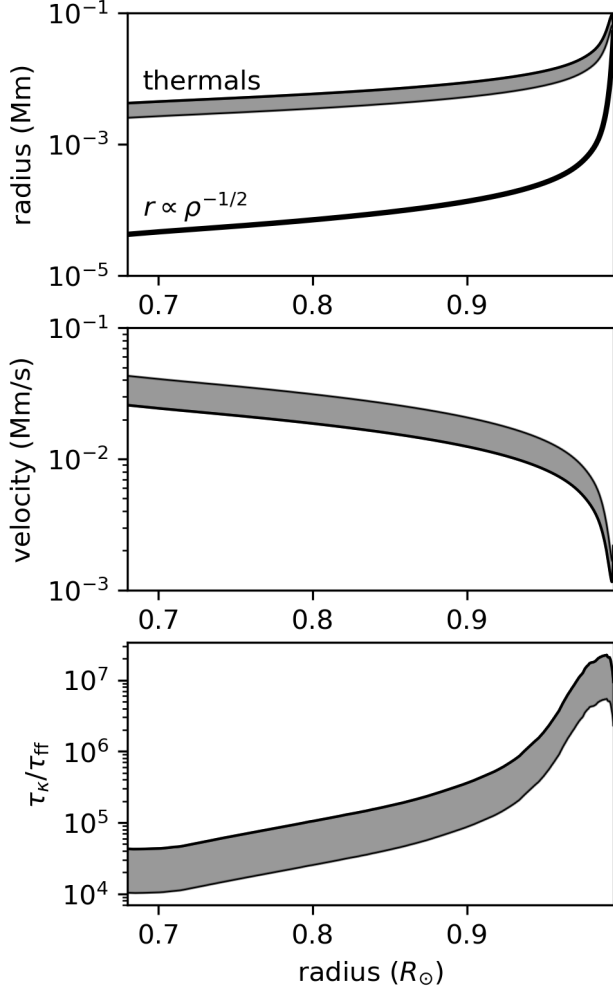


Figure 6. (a) Bounds on the evolution of the radii of entropy rain in the Sun are shown and compared to what the radii would be under purely horizontal compression. (b) The velocities of the thermals in the estimated boundaries are shown. (c) The estimated ratio of the thermal diffusion timescale of the thermals normalized by the thermal’s freefall timescale over 1 Mm is shown. Diffusivities are calculated using the realistic solar-like diffusion profiles of [Brown \(2011\)](#).

APPENDIX

A. THERMAL MEASUREMENTS

Throughout this work, we frequently report the thermal’s radius or its depth. We measure the thermal’s radius and height as the radius from the axis of symmetry and the height from the bottom of the domain at which the thermal’s vortex core is located. To measure this, we locate the maxima of the entropy. To find the entropy maxima vertically, we integrate $\int \rho S_1 r dr$ in our Dedalus domain, then use the spectral data of that profile to sample it on a 4096 point grid vertically, and we take the location of the minima on that grid to be the thermal height. To find the entropy maxima horizontally, we integrate $\int \rho S_1 dz$ in our Dedalus domain, then sample the spectral data onto a 2048-point radial grid, and take the minima of that profile to be the radius of the thermal. In order to find the thermal’s velocity

Table 2. Table of simulation information

| n_ρ | nr or nx = ny | nz | $t_{\text{evolution}}$ | safety |
|--|---------------|------|------------------------|--------|
| 2D Anelastic Simulations | | | | |
| 0.1 | 128 | 512 | 50 | 0.6 |
| 0.5 | 128 | 512 | 45 | 0.6 |
| 1 | 128 | 512 | 41 | 0.6 |
| 2 | 128 | 1024 | 34 | 0.4 |
| 3 | 192 | 1024 | 29 | 0.4 |
| 4 | 256 | 1024 | 26 | 0.3 |
| 5 | 256 | 1536 | 25 | 0.14 |
| 6 | 256 | 1536 | 23 | 0.08 |
| 3D Fully Compressible Simulations | | | | |
| 0.1 | 256 | 512 | 50 | 0.15 |
| 0.5 | 256 | 512 | 45 | 0.15 |
| 1 | 256 | 512 | 41 | 0.15 |
| 2 | 256 | 1536 | 34 | 0.1 |

NOTE—

as a function of time, we use a five-point stencil to differentiate the thermal’s depth, d ,

$$w_{\text{th}}(t) = \frac{d}{dt}d_{\text{th}}(t) = \frac{-d_{\text{th}}(x + 2\Delta t) + 8d_{\text{th}}(t + \Delta t) - 8d_{\text{th}}(t - \Delta t) + d_{\text{th}}(t - 2\Delta t)}{12\Delta t}$$

Integral quantities, such as the circulation, Γ , the buoyancy, B , and the volume, \mathcal{V} require us to first determine what fraction of the domain constitutes the thermal. To do so, we use the thermal tracking algorithm described in appendix B to determine the radial contour that outlines the thermal as a function of height, \mathcal{C} . We then use this contour to find our integral quantities,

$$\Gamma = \int_0^{\mathcal{C}} \int_0^{L_z} (\nabla \times \mathbf{u})_\phi dz dr, \quad B = 2\pi \int_0^{\mathcal{C}} \int_0^{L_z} \rho S_1 r dz dr, \quad \mathcal{V} = 2\pi \int_0^{\mathcal{C}} \int_0^{L_z} r dz dr. \quad (\text{A1})$$

B. THERMAL TRACKING

We use a thermal tracking algorithm very similar to the one used in Lecoanet & Jeevanjee (2018) and inspired by the work of Romps & Charn (2015) in order to determine the full extent of the thermal, as pictured by the elliptical outlines in Fig. 2 We begin by measuring the thermal’s velocity versus time, w_{th} , as described in appendix A. We then calculate the streamfunction of the velocity field as in Romps & Charn (2015),

$$\frac{\partial \psi}{\partial r} = 2\pi \rho r (w - w_{\text{th}}), \quad (\text{B2})$$

with the boundary condition that $\psi = 0$ at $r = 0$. The contour defined by $\psi = 0$ from this solution is taken to be the contour bounding the thermal, \mathcal{C} .

C. TABLE OF SIMULATIONS

Information regarding the simulation resolution and CFL safety factor for each of the simulations presented in this work is contained in table 2. The Python scripts used to perform all simulations and analysis in this work are stored online in a Zenodo repository CITE.

REFERENCES

- | | |
|--|--|
| <p>Akhmetov, D. G. 2009, Vortex rings (Berlin, Heidelberg: Springer Berlin Heidelberg), 1–151, doi:10.1007/978-3-642-05016-9</p> | <p>Anders, E. H., & Brown, B. P. 2017, Physical Review Fluids, 2, 083501</p> |
|--|--|

- Ascher, U. M., Ruuth, S. J., & Spiteri, R. J. 1997, *Applied Numerical Mathematics*, 25, 151
- Avrett, E. H., & Loeser, R. 2008, *ApJS*, 175, 229
- Borrero, J. M., & Bellot Rubio, L. R. 2002, *A&A*, 385, 1056
- Brandenburg, A. 2016, *ApJ*, 832, 6
- Brown, B. 2011, in *Journal of Physics Conference Series*, Vol. 271, GONG-SoHO 24: A New Era of Seismology of the Sun and Solar-Like Stars, 012064
- Burns, K., Vasil, G., Oishi, J., Lecoanet, D., & Brown, B. 2016, *Dedalus: Flexible framework for spectrally solving differential equations*, *Astrophysics Source Code Library*, , ascl:1603.015
- Burns, K. J., Vasil, G. M., Oishi, J. S., Lecoanet, D., & Brown, B. P. 2019, *arXiv e-prints*, arXiv:1905.10388
- Cossette, J.-F., & Rast, M. P. 2016, *ApJ*, 829, L17
- Featherstone, N. A., & Hindman, B. W. 2016, *ApJ*, 830, L15
- Greer, B. J., Hindman, B. W., Featherstone, N. A., & Toomre, J. 2015, *ApJ*, 803, L17
- Hanasoge, S. M., Duvall, T. L., & Sreenivasan, K. R. 2012, *Proceedings of the National Academy of Science*, 109, 11928
- Hotta, H. 2017, *ApJ*, 843, 52
- Käpylä, P. J., Rheinhardt, M., Brandenburg, A., et al. 2017, *ApJ*, 845, L23
- Lecoanet, D., Brown, B. P., Zweibel, E. G., et al. 2014, *ApJ*, 797, 94
- Lecoanet, D., & Jeevanjee, N. 2018, *arXiv e-prints*, arXiv:1804.09326
- Morton, B. R., Taylor, G., & Turner, J. S. 1956, *Proceedings of the Royal Society of London Series A*, 234, 1
- O'Mara, B., Miesch, M. S., Featherstone, N. A., & Augustson, K. C. 2016, *Advances in Space Research*, 58, 1475
- Paxton, B., Bildsten, L., Dotter, A., et al. 2011, *ApJS*, 192, 3
- Romps, D. M., & Charn, A. B. 2015, *Journal of the Atmospheric Sciences*, 72, 2890
- Romps, D. M., & Charn, A. B. 2015, *Journal of Atmospheric Sciences*, 72, 2890
- Scorer, R. S. 1957, *Journal of Fluid Mechanics*, 2, 583
- Shivamoggi, B. K. 2010, *Physics Letters A*, 374, 4736
- Spruit, H. C. 1997, *Mem. Soc. Astron. Italiana*, 68, 397
- Tarshish, N., Jeevanjee, N., & Lecoanet, D. 2018, *Journal of Atmospheric Sciences*, 75, 3233
- Wang, D., & Ruuth, S. J. 2008, *Journal of Computational Mathematics*, 26, 838